applied optics

Performance evaluation of a two detector camera for real-time video

Benjamin Lochocki,* Adrián Gambín-Regadera, and Pablo Artal

Laboratorio de Óptica, Universidad de Murcia, Campus de Espinardo (Edificio 34), Murcia 30100, Spain
**Corresponding author: benjamin@um.es*

Received 22 July 2016; revised 7 November 2016; accepted 15 November 2016; posted 16 November 2016 (Doc. ID 270914); published 13 December 2016

Single pixel imaging can be the preferred method over traditional 2D-array imaging in spectral ranges where conventional cameras are not available. However, when it comes to real-time video imaging, single pixel imaging cannot compete with the framerates of conventional cameras, especially when high-resolution images are desired. Here we evaluate the performance of an imaging approach using two detectors simultaneously. First, we present theoretical results on how low SNR affects final image quality followed by experimentally determined results. Obtained video framerates were doubled compared to state of the art systems, resulting in a framerate from 22 Hz for a 32 × 32 resolution to 0.75 Hz for a 128 × 128 resolution image. Additionally, the two detector imaging technique enables the acquisition of images with a resolution of 256 × 256 in less than 3 s.

OCIS codes: (110.0110) Imaging systems; (110.1758) Computational imaging; (230.6120) Spatial light modulators.

https://doi.org/10.1364/AO.55.010198

1. INTRODUCTION

Single pixel imaging, or computational imaging, refers to a technique where either the image of the object is modulated in the focal plane ("backward scheme") or the object is illuminated by spatially coded patterns ("forward scheme"). For each pattern, the reflected or transmitted intensity is measured using a single detector, also called bucket collector, for example, a photodiode or a photomultiplier. Once a finite amount of patterns has been projected on the object, an image of the object can be reconstructed based on the projected patterns and their corresponding intensity. This approach is suitable for imaging in the visible or infrared spectrum, in a terahertz environment, for 2D or 3D imaging, in low light conditions, in microscopic or natural scene environments, for grayscale and color imaging [1–6]. Single pixel imaging might have the advantage to overcome scattering when traversing through opaque media [3,7] and enable imaging in spectral ranges where 2D-array cameras are not available.

The projected patterns can be based on the noiselet transform [8,9], on the discrete cosine transform [9], or they could be random binary [10] or grayscale sinusoidal patterns [11]. Here, patterns based on the Hadamard transform [12–14] are used, as utilized by many others [5,7,15–17]. The so-called Hadamard patterns are easy to compute from a base $N \times N$ Walsh–Hadamard matrix, which is also straightforward to generate. Additionally, the patterns are binary and therefore suitable for display on a digital micromirror device (DMD), and they are considered to have the optimum design of an equally weighted distribution of black and white pixels (except for the first pattern where all pixels are white).

To obtain an image with a resolution of $N \times N$, N^2 patterns need to be projected to fully reconstruct the object. The binary mathematical model of the Hadamard patterns consists of positive and negative ones (+1, −1). A DMD is able to display binary patterns in that sense of "on" and "off," basically 1 and 0, but not negative values. Therefore, it is recommended to display not only one Hadamard pattern but also the inverted counterpart to achieve the response of the negative when using a single pixel setup. Most groups accomplish that by displaying a pattern and successively the inverted complement [7,15,18], which leads to a significant decrease in noise even when the measurements are performed successively and not at the exact time. However, the main disadvantage is the doubling of the patterns displaying time because now a set of $2 \times N^2$ needs to be displayed and this time is limited by the framerate of the DMD. However, imaging time might be a crucial factor when imaging at high resolutions if the lifetime of an object is short or the object in constant motion. A solution to decrease imaging time can be the utilization of a balanced detector [19] or the implementation of a second detector [20,21]. Here, we are pushing the hardware to current limitations in terms of imaging and reconstruction speed for N up to 256. Furthermore, we demonstrate the maximum possible in terms of real-time video streams for various resolutions. For readers new to the

topic of single pixel imaging, we offer noise simulations, which might help to understand why the use of the differential Hadamard pattern single pixel imaging approach is recommended.

2. EXPERIMENTAL SYSTEM

A simple imaging system was built as depicted in Fig. 1. The object, a Siemens star printed on transparent paper and inserted into black paper to block unwanted light into the system, is back illuminated homogenously using a liquid fiber coming from a broadband Xenon lamp (Hamamatsu L7810-02). This light source was favored for the constant power output over time, which is crucial when measuring small discrete amplitude modulations coming from the structured illumination of the object. The object is imaged onto the DMD using a lens, f1, in a 2f configuration ("backward scheme"). The employed DMD (Vialux V-7001, controller board V4395, chipset DLP 4100, pixel size: 13.68 µm, resolution: 1024 × 768, and memory: 8GB) can store up to 87380 binary patterns and has a maximum display rate of 22.727 kHz. The Hadamard patterns are created on the computer and transferred through a USB 3.0 connection into the memory of the DMD. From the memory of the DMD controller board, the patterns are constantly available and can be displayed in an instant. In this study, the display rate of the DMD was always at the maximum because the main purpose of this study is real-time imaging.

Next, the set of patterns is displayed on the DMD. The Hadamard patterns are scaled to 512 × 512 pixels on the DMD (around 7 × 7 mm), meaning one pixel of a 32 × 32 Hadamard pattern resembles 16 × 16 pixel on the DMD, one pixel in a 64 × 64 pattern resembles 8 × 8 pixels on the DMD, and so on.

Since a DMD has only two states: reflecting light into one direction or another, each detector (d1: Thorlabs PDA36; d2: Thorlabs PDA100; both operating with the 10 db gain setting) is placed with a condenser lens (f2 = f3 = 25 mm) at each deflection path. That means that while displaying a binary pattern on the DMD, the "white" or "1" parts of the pattern are reflected into d1, while the "black" or "0" pixels are reflected into d2. Further, the detectors are synchronized with the framerate of the DMD, so that for each projected pattern a positive

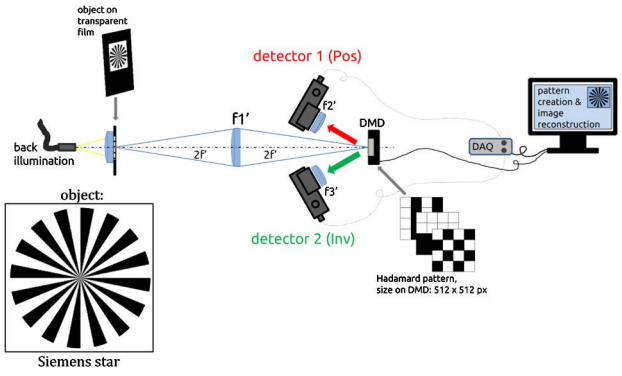

Fig. 1. Experimental system used to image a back illuminated object (inset: Siemens star) onto the DMD with a lens f1. The detectors d1 and d2 collect the reflected light coming from the DMD.

and "negative" measurement is received. The measured intensity of both detectors is transferred via an analog-to-digital converter (National Instruments PCIe-6361 with a maximum sampling rate of 2 MS/s; for two or more detectors the sampling rate is reduced to 500 kS/s) to a PC. This allows for 21 measurements per pattern while running the DMD at the maximum frequency of 22.727 kHz. Not all data is used for further processing. Data from the start and the end of each pattern measurement were removed because it was affected by tiny wiggles coming from the settling time of the mirrors. The remaining 17 measurements per pattern were averaged and result in one intensity measurement per pattern. Before further proceeding, the average of the negative data is matched with the average of the positive data by a simple factor. This step is necessary because the negative data is contaminated with constant background light coming from the "0" pixels around the Hadamard pattern. Normalization of the data is recommend to enhance image reconstruction [22–24]. Subsequently, the negative data is subtracted from the corresponding positive data and saved as final intensity measurement per pattern, intensity_i, which corresponds to the mathematical Hadamard pattern description. From there an image of the object can be reconstructed using the equation:

$$\text{Image}(m, n) = \sum_{i}^{N^2} \text{intensity}_i \times \text{pattern}_i(m, n), \quad (1)$$

where $\text{pattern}_{m,n}$ (m and n are pixel values in a $N \times N$ Hadamard pattern matrix consisting of "+1s" and "−1s") is reformatted to pattern_i. Each intensity_i is multiplied by each element of the corresponding pattern_i, which results in a sub-image. The sum of all sub-images adds up to the final image.

3. RESULTS AND DISCUSSION

The following images and videos were obtained from our in-house developed software written in C++ and running on a desktop PC (i5-4590, quad-core, 3.3 GHz, 8 GB Ram). The software is capable of reconstructing individual images and composing real-time videos in an instant. Basic filters including interpolation, contrast stretching and scaling could be applied to improve visibility. Eventually, the reconstructed images and videos obtained with $N = 32$, 64, and 128 were scaled (not interpolated) to a size of 256 × 256 for viewing purposes, and the images and videos are saved. Additionally, it is worth mentioning that the experiment in this study took place in a dark environment, and the setup was completely covered. The SNR was high due to the direct illumination of the object with the fiber tip and hence the direct imaging onto the DMD. We performed the experiments with the laboratory lights on and obtained similar results. Therefore, the impact of noise introduced by an external light source, such as the two detectors themselves or background light from the light source, any computer monitor, or status LED, can be neglected in this study. However, the next paragraph presents a more detailed analysis of the impact of noise.

A. Dealing with Noise

One could argue that it is sufficient to display only the N^2 set of pattern (without the inverted complement) as it is possible to

simulate or calculate the inverted counterpart. This can be performed either by plainly subtraction the mean of all intensities from all individual intensities [5,25] or by calculating the theoretical intensity value of the inverted pattern if one knows the intensity of the first, full white, pattern. For demonstration purposes, we will focus on the first simulation method and subtract the mean value from all obtained measurements. In what follows, we call this method A, and displaying the positives and the inverted complement patterns refers to method B.

We used the object in Fig. 2, which has the size of 4×4 pixel and four different gray values in no particular order. Figure 3 shows a comparison of the obtained values after the intensity of the object was measured by $N^2 = 16$ patterns. The upper row shows the values and the corresponding pattern for method A where white equals +1 and black equals 0. The second row shows values of method B where white pixels are +1 and black pixels equal −1.

Simulating the inverted patterns leads to positive and negative intensity values (before, all intensity measurements were positive because only positive values can be measured). Figure 4 displays the data obtained with method A: the graph (a) shows the positive data and (b) the data after the subtraction of the mean. Data from method B are shown in graph (c) as the green curve, and graph (d) illustrates the numerical difference between both methods. In Fig. 4, the overall curve of graphs (b) and (c) resemble the same trend but differ by a factor 2. However, a reconstruction of the object is perfectly possible. Unfortunately, there is no perfect system and noise is a steady companion. Noise can be introduced by the photodetector, the light source, and background illumination (PC monitor, status

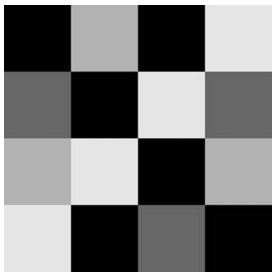

Fig. 2. Test image with four grayscale values used during simulation.

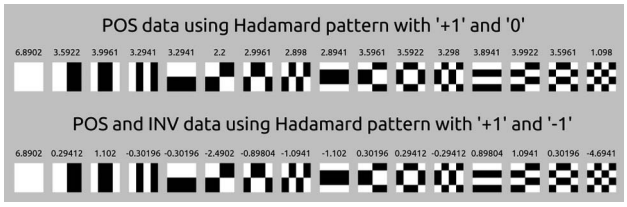

Fig. 3. Results of $N^2 = 16$ patterns measuring the test object displayed in Fig. 2. The first row indicates the measurements performed with only positive (+1 and 0) patterns where only positive values are measured (intensity values above each pattern). The second row shows the received measurements from positive and inverted (+1 and −1) patterns and the corresponding intensity values.

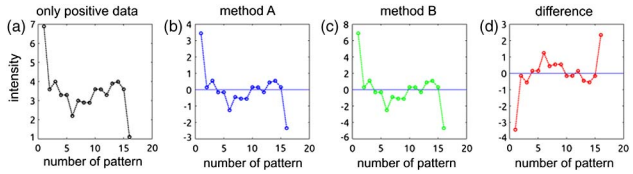

Fig. 4. (a) Intensity data of 16 positive Hadamard patterns. (b) Data of (a) after the mean is subtracted. (c) Data of 16 positive and inverted Hadamard patterns. (d) The difference between the simulated data of (b) and the real data of (c).

LEDs, and laboratory lights) and can be divided in instrument and photon noise. For readers with further interest in the impact of noise in a Hadamard imaging system, we recommend the following reference where the topic is discussed in great detail [26]. Here, we show in brief, a comparison of how noise influences the outcome of the measurements in both methods.

Figure 5 is similar to Fig. 4 with additionally introduced Gaussian white noise to both methods using the "awgn" function in the MATLAB software package. This type of noise simulates the fluctuation in illumination levels between each pattern and is therefore preferred to Poisson noise, which would be the preferred method to simulate detector noise.

The first row of Fig. 5 shows data where noise was added to the signal when using method A. SNR 20 is considered to be a good signal in image processing. The signal is clearly superior to the noise and therefore similar compared to the original signal, and the differences between the original signal and the noisy signal are small (the red graphs). As more noise is added, the original signal gets more and more altered, and the noise has a severe impact and differences are hard to ignore, particularly when looking at data from method A. In Fig. 6, the results of the reconstructed images are depicted as more noise was added to the signal, and clearly show the emerging issue with method A. Method A might be a valid approach as long as the system contains a minimum of noise. Noise levels will be reduced to a minimum if during the illumination of the object the inverted patterns are displayed [27]. It is reasonable to display each inverted pattern successively after the corresponding positive pattern (and not after all N^2 positive patterns). Therefore, it is highly recommended to use method B to improve imaging quality, especially while working in low light

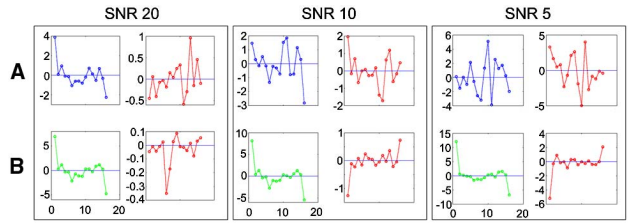

Fig. 5. Three simulations where different Gaussian white noise is added to the original signal [graphs 4(b) and 4(c)]. The first row displays the original signal with the added noise (blue) and the difference to the original signal (red) for method A. The bottom row shows the original signal with added noise for method B (green) and the difference from the original signal (red). Please note the difference in the y-axis scale.

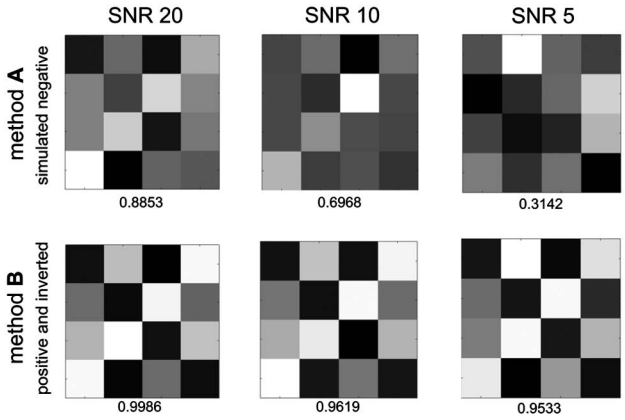

Fig. 6. Reconstructed images after noise is introduced. The top row shows the reconstructed images using method A, and the bottom row when method B is used. The numbers below the images show the correlation coefficient compared to the reference image in Fig. 2, based on Eq. (3) of [19].

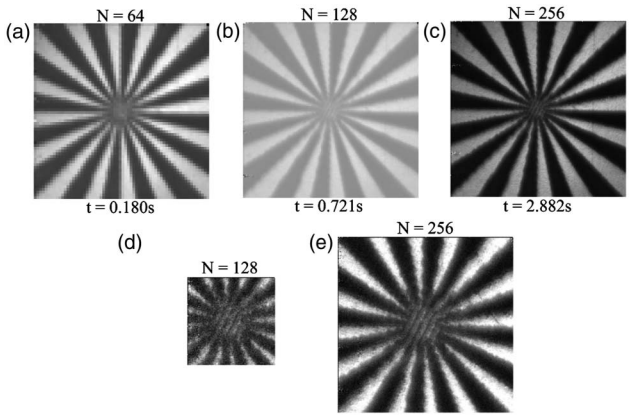

Fig. 8. Image reconstruction for (a) $N = 64$, (b) $N = 128$, and (c) $N = 256$. All images are up-scaled to 256 × 256 px (except images with $N = 256$). Imaging time is indicated. Images (d) and (e) are reconstructed with maximum resolution, 1 px ≃ 13.68 μm.

conditions as on a single photon level where photomultiplier tubes are used [28], and where high acquisition rates are desired and hence the integration time of the detector is kept to a minimum as during real-time imaging. One additional method to increase the acquisition time and therefore lower the imaging time could be the division of the used spatial illumination into sub-patterns and hence the parallel detection of the sub-pattern intensities using an array of detectors [29].

B. Full Resolution Image Reconstruction

To obtain a single image, one begins by displaying of all patterns. The software reads the data of both detectors, which is automatically followed by the subtraction of both received data sets and the immediate reconstruction of the image of the object.

Figure 7 depicts the image reconstruction of an object using $N = 32$ patterns, and the imaging time is $t = 0.045$ s. The figure shows the comparison of a reconstructed image from positive data received via d1 (on the left), the reconstructed image from negative data received via d2 (in the center), and the reconstructed image from intensity$_i$, after the subtraction of the negative data of d2 from the positive data of d1. It can be clearly seen that the image on the right side, (c), contains

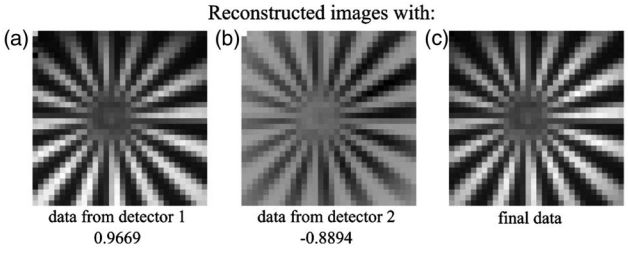

Fig. 7. Reconstructed images for $N = 32$, up-sampled to 256 × 256 px. (a) Positive detector. (b) Negative detector. (c) Reconstruction after the negative data is subtracted from the positive data, resulting in a higher contrast image with fewer artifacts. Correlation coefficient below the images compared to (c).

less artifacts compared to the former images, especially when one looks at the first column. Moreover, contrast is improved too. This supports the necessity of displaying the pattern and the inverted complements on a DMD to avoid a loss in image quality.

Some might argue that the left image in Fig. 7 is already a suitable reconstruction, and we remind those that these results were obtained in a low noise environment and the SNR was high. Working in a noisy environment or on a single photon level would not lead to such a great quality of the reconstructed image [15,28,30–32], as shown in the previous paragraph. In addition, while using two detectors tinkering with the 1st pixel can be avoided, a common task during single pixel imaging.

While the reconstructed images for $N = 32$ and 64 are displayed in an instant, images with higher resolution $N \geq 128$ take a few seconds to be reconstructed due to the amount of data that needs to be processed. In Figs. 8(a)–8(c) experimental results for different Ns are shown. Due to the use of a second detector, it is also possible to create an $N = 256$ image as now all required patterns ($N^2 = 65536$) can be loaded into the memory of the DMD. Additionally, images in Figs. 8(d) and 8(e) are reconstructed with the maximum possible resolution where one pixel in the pattern resembles one pixel on the DMD, giving a resolution of 1 px ≃ 13.68 μm.

In Table 1, a comparison of theoretical and experimentally obtained FPS are shown for various resolutions. For higher resolution, a larger number of patterns have to be displayed and therefore a decrease in FPS is obtained. The flaw of high-resolution real-time imaging is the gap between theoretical and experimentally obtained FPS. This is because of the exponential growth of data, which needs to be acquired and processed by the computer before the imaging procedure can be repeated.

The presented system configuration clearly exhibits improvement to real-time video rate. Videos for $N = 32$ (Visualization 1), 64 (Visualization 2) and 128 (Visualization 3) can be found online in the supplementary section, using the same experimental system but direct illumination of the object (a measurement tape). Compared to

Table 1. Comparison of Theoretical and Experimentally Obtained FPS

N	32	64	128	256
Number of pattern: 2 detectors (1 detector)	1024 (2048)	4096 (8192)	16384 (32768)	65536 (-)
Time to display: N^2 ($2 \times N^2$) pattern in s	0.045 (0.090)	0.180 (0.360)	0.721 (1.442)	2.882 (-)
Theoretical FPS[a] 2 detectors (1 detector)	22.19 (11.10)	5.55 (2.77)	1.39 (0.69)	0.35 (0.17)
Experimental FPS	22.19	5.50	0.75	0.04
FPS obtained by others, using 1 detector	10 [15,16,33]	2.5 [15,16,33,34]	0.5 [19]	-

[a]Without computational reconstruction time, solely displaying time of the patterns with maximum DMD frequency.

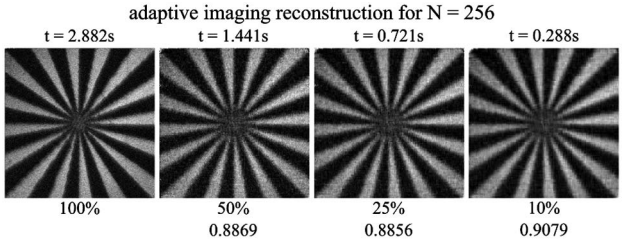

Fig. 9. Adaptive imaging results for $N = 256$. t is the time, which is needed to display the percentage of pattern. The numbers in the last row are the correlation coefficients compared to the first image (100%).

systems where one single detector is employed and the patterns are displayed with inverse complements, the FPS is doubled.

For $N \geq 128$, the framerate is increased but the anticipated doubling is not reached. As an example, for $N = 256$, the illumination time to display all required patterns was around 3 s, though the image reconstruction takes around 22 s, which results in an overall FPS of 0.04. This is because of the vast amount of data that needs to be processed to reconstruct the full resolution image, even though the calculations are very basic, the software is optimized to make use of the full potential of the available CPU.

C. Adaptive Image Reconstruction

A technique to further improve the video framerate is to reduce the number of patterns after intensity measurements of a complete set of patterns (N^2) are performed. The intensity measurements are subsequently sorted by means of the highest response. From there, only a fraction of highly responsive patterns are chosen. This is known as adaptive imaging or evolutionary compressive sensing [16,34]. Subsequently, this set of patterns (which can be significant smaller than N^2) is displayed, the intensities measured, and an image reconstructed. The reduced number of patterns can be sufficient to reconstruct an object in great detail [16,22] as shown in Fig. 9. Ideally, when the number of patterns is reduced and the imaging time is decreased, higher video framerates should be obtained. In our study this is only partially the case, as image reconstruction time for $N = 256$ stays almost constant during a 50% reduction, as seen in Table 2. In the future, more powerful hardware (GPU instead of CPU) might decrease computational time and therefore higher real-time video framerates will be possible. Nevertheless, as soon as the area of interest changes (or the object moves), this approach will stop working because each object or scene has an individual set of high responsive patterns and therefore the intensities of a complete set of patterns need to be measured prior to lowering the number of patterns again.

Table 2. T(heoretical) Versus E(xperimental) FPS Results While Applying Adaptive Imaging Using Two Detectors

	$N = 32$		$N = 64$		$N = 128$		$N = 256$	
%	T	E	T	E	T	E	T	E
100	22.19	22.19	5.55	5.50	1.38	0.75	0.34	0.04
75	29.59	29.59	7.40	7.34	1.84	1.03	0.45	0.05
50	44.39	44.39	11.10	11.10	2.77	1.53	0.69	0.07
25	88.78	88.78	22.19	22.12	5.55	3.01	1.38	0.18
10	220	220	55.49	55.45	13.87	7.34	3.46	0.46

4. CONCLUSION

The use of two detectors in a single pixel imaging related system halves the pattern projection time while maintaining image quality and therefore doubling the framerate for real-time video imaging. Further increase can be accomplished by using adaptive imaging techniques. Moreover, the proposed method enables computational images for a resolution of 256 × 256 px within 2.88 s. The proposed solution significantly decreases the overall imaging duration within a multiplexed illumination system when used in a configuration where the object is imaged onto the DMD plane. If one implements the imaging path vice versa by imaging the DMD plane onto the object ("forward scheme") this approach has limitations. In that kind of configuration, it would not be possible to employ a second detector to measure the inverted intensity at the same time. However, there might be other solutions, like using two light sources with different polarization or wavelength, both illuminating the DMD from opposite directions and their beams are combined on the object plane. This would mean, the object is always completely illuminated since one half of the pixels are the positive 1s of one source and at the same time the negative 1s of the other source and vice versa. Two detectors could collect the reflected light with different polarization or wavelength filters. One would have to tinker with the alignment on the object plane where both beams need to be combined precisely without the slightest overlapping.

However, customized hardware, especially a squared micro mirror array (e.g., 512 × 512 px) could first increase the DMD framerate, which would increase the real-time video framerate by lowering the overall imaging time. Second, it would avoid the contamination of the second detector with light coming

from the background pixels outside the Hadamard area pointing toward detector two.

These type of two detector approach could have some potential benefit in applications where speed is a requirement as in retinal imaging [35].

Funding. European Research Council (ERC) (ERC-2013-AdG-339228 [SEECAT]).

Acknowledgment. We would like to thank Esther Irles, Enrique Tajahuerce, and Jesus Lancis from the Institute of New Imaging Technologies, Castellon, Spain, for helpful discussions.

REFERENCES

1. X. Miao and B. Amirparviz, "Single pixel camera," U.S. patent US20150042834 A1 (12 February 2015).
2. H. Yu, Y. Liu, Y. Peng, W. Xu, and M. Zhang, "A portable single-pixel camera based on coarse-to-fine coding light," in *IEEE International Conference on Imaging Systems and Techniques (IST)* (2015), pp. 1–5.
3. R. I. Stantchev, B. Sun, S. M. Hornett, P. A. Hobson, G. M. Gibson, M. J. Padgett, and E. Hendry, "Non-invasive, near-field terahertz imaging of hidden objects using a single pixel detector," arXiv (2015).
4. S. J. Olivas, Y. Rachlin, L. Gu, B. Gardiner, R. Dawson, J. P. Laine, and J. Ford, *Single Pixel Compressive Imaging of Laboratory and Natural Light Scenes* (2013).
5. M. F. Duarte, M. A. Davenport, D. Takhar, J. N. Laska, T. Sun, K. F. Kelly, and R. G. Baraniuk, "Single-pixel imaging via compressive sampling," IEEE Signal Process. Mag. **25**(2), 83–91 (2008).
6. B. Sun, M. P. Edgar, R. Bowman, L. E. Vittert, S. Welsh, A. Bowman, and M. J. Padgett, "3D computational imaging with single-pixel detectors," Science **340**, 844–847 (2013).
7. E. Tajahuerce, V. Durán, P. Clemente, E. Irles, F. Soldevila, P. Andrés, and J. Lancis, "Image transmission through dynamic scattering media by single-pixel photodetection," Opt. Express **22**, 16945–16955 (2014).
8. R. Coifman, F. Geshwind, and Y. Meyer, "Noiselets," Appl. Comput. Harmon. Anal. **10**, 27–44 (2001).
9. E. Candès and J. Romberg, "Sparsity and incoherence in compressive sampling," Inverse Probl. **23**, 969–985 (2007).
10. M. B. Wakin, J. N. Laska, M. F. Duarte, D. Baron, S. Sarvotham, D. Takhar, K. F. Kelly, and R. G. Baraniuk, "An architecture for compressive imaging," in *International Conference on Image Processing* (IEEE, 2006), pp. 1273–1276.
11. Z. Zhang, X. Ma, and J. Zhong, "Single-pixel imaging by means of Fourier spectrum acquisition," Nat. Commun. **6**, 1–6 (2015).
12. W. K. Pratt, J. Kane, and H. C. Andrews, "Hadamard transform image coding," Proc. IEEE **57**, 58–68 (1969).
13. C. F. Chen and W. K. Leung, "Algorithms for converting sequence-, dyadic-, and Hadamard-ordered Walsh functions," Math. Comput. Simul. **27**, 471–478 (1985).
14. T. Ritter, "Walsh–Hadamard transforms: a literature survey," http://www.ciphersbyritter.com/RES/WALHAD.HTM.
15. M. P. Edgar, G. M. Gibson, R. W. Bowman, B. Sun, N. Radwell, K. J. Mitchell, S. S. Welsh, and M. J. Padgett, "Simultaneous real-time visible and infrared video with single-pixel detectors," Sci. Rep. **5**, 10669 (2015).
16. N. Radwell, K. J. Mitchell, G. M. Gibson, M. P. Edgar, R. Bowman, and M. J. Padgett, "Single-pixel infrared and visible microscope," Optica **1**, 285–289 (2014).
17. K. Nitta, S. Hayashi, and O. Matoba, "Divided Hadamard pattern illumination for fewer times measurements," Work. Inf. Opt. **20152**, 1–3 (2015).
18. M. J. Sun, M. P. Edgar, D. B. Phillips, G. M. Gibson, and M. J. Padgett, "Improving the signal-to-noise ratio of single-pixel imaging using digital microscanning," Opt. Express **24**, 10476–10485 (2016).
19. F. Soldevila, P. Clemente, E. Tajahuerce, N. Uribe-Patarroyo, P. Andrés, and J. Lancis, "Computational imaging with a balanced detector," Sci. Rep. **6**, 29181 (2016).
20. W. K. Yu, X. F. Liu, X. R. Yao, C. Wang, Y. Zhai, and G. J. Zhai, "Complementary compressive imaging for the telescopic system," Sci. Rep. **4**, 5834 (2014).
21. R. G. Baraniuk, K. F. Kelly, R. F. Bridge, S. Chatterjee, and L. McMackin, "Dual-port measurements of light reflected from micromirror array," U.S. patent 8717466 B2 (4 September, 2014).
22. S. S. Welsh, M. P. Edgar, R. Bowman, P. Jonathan, B. Sun, and M. J. Padgett, "Fast full-color computational imaging with single-pixel detectors," Opt. Express **21**, 23068–23074 (2013).
23. B. Sun, S. S. Welsh, M. P. Edgar, J. H. Shapiro, and M. J. Padgett, "Normalized ghost imaging," Opt. Express **20**, 16892–16901 (2012).
24. F. Ferri, D. Magatti, L. A. Lugiato, and A. Gatti, "Differential ghost imaging," Phys. Rev. Lett. **104**, 1–4 (2010).
25. J. Wang, M. Gupta, and A. C. Sankaranarayanan, "LiSens—A scalable architecture for video compressive sensing," arXiv (2015).
26. L. Streeter, G. R. Burling-Claridge, M. J. Cree, and R. Künnemeyer, "Optical full Hadamard matrix multiplexing and noise effects," Appl. Opt. **48**, 2078–2085 (2009).
27. W. K. Yu, X. R. Yao, X. F. Liu, R. M. Lan, L. A. Wu, G. J. Zhai, and Q. Zhao, "Compressive microscopic imaging with "positive-negative" light modulation," Opt. Commun. **371**, 105–111 (2016).
28. A. D. Rodríguez, P. Clemente, E. Irles, E. Tajahuerce, and J. Lancis, "Resolution analysis in computational imaging with patterned illumination and bucket detection," Opt. Lett. **39**, 3888–3891 (2014).
29. J. P. Dumas, M. A. Lodhi, W. U. Bajwa, and M. C. Pierce, "Computational imaging with a highly parallel image-plane-coded architecture: challenges and solutions," Opt. Express **24**, 6145–6155 (2016).
30. R. M. Willett, R. F. Marcia, and J. M. Nichols, "Compressed sensing for practical optical imaging systems: a tutorial," Opt. Eng. **50**, 72601–72613 (2011).
31. K. Shibuya, K. Nakae, Y. Mizutani, and T. Iwata, "Comparison of reconstructed images between ghost imaging and Hadamard transform imaging," Opt. Rev. **22**, 897–902 (2015).
32. K. Guo, S. Jiang, and G. Zheng, "Multilayer fluorescence imaging on a single-pixel detector," Biomed. Opt. Express **7**, 2425–2431 (2016).
33. N. Huynh, E. Zhang, M. Betcke, S. Arridge, P. Beard, and B. Cox, "Single-pixel optical camera for video rate ultrasonic imaging," Optica **3**, 26–29 (2016).
34. M. J. Sun, M. P. Edgar, G. M. Gibson, B. Sun, N. Radwell, R. Lamb, and M. J. Padgett, "Single-pixel 3D imaging with time-based depth resolution," Nat. Commun. **7**, 1–10 (2016).
35. B. Lochocki, A. Gambín, S. Manzanera, E. Irles, E. Tajahuerce, J. Lancis, and P. Artal, "Single pixel camera ophthalmoscope," Optica **3**, 1056–1059 (2016).